ACS Catalysis

Research Article

pubs.acs.org/acscatalysis

Anionic Group Self-Doping as a Promising Strategy: Band-Gap Engineering and Multi-Functional Applications of High-Performance CO_3^{2-}-Doped $Bi_2O_2CO_3$

Hongwei Huang,[*,†] Xiaowei Li,[†] Jinjian Wang,[†] Fan Dong,[*,‡] Paul K. Chu,[§] Tierui Zhang,[£] and Yihe Zhang[*,†]

[†]Beijing Key Laboratory of Materials Utilization of Nonmetallic Minerals and Solid Wastes, National Laboratory of Mineral Materials, School of Materials Science and Technology, China University of Geosciences, Beijing 100083, China

[‡]Chongqing Key Laboratory of Catalysis and Functional Organic Molecules, College of Environmental and Bio-logical Engineering, Chongqing Technology and Business University, Chongqing, 400067, China

[§]Department of Physics and Materials Science, City University of Hong Kong, Tat Chee Avenue, Kowloon, Hong Kong, China

[£]Key Laboratory of Photochemical Conversion and Optoelectronic Materials, Technical Institute of Physics and Chemistry, Chinese Academy of Sciences, Beijing 100190, China

Supporting Information

ABSTRACT: We herein demonstrate self-doping of the CO_3^{2-} anionic group into a wide bandgap semiconductor $Bi_2O_2CO_3$ realized by a one-pot hydrothermal technique. The photoresponsive range of the self-doped $Bi_2O_2CO_3$ can be extended from UV to visible light and the band gap can be continuously tuned. Density functional theory (DFT) calculation results demonstrate that the foreign CO_3^{2-} ions are doped in the caves constructed by the four adjacent CO_3^{2-} ions and the CO_3^{2-} self-doping can effectively narrow the band gap of $Bi_2O_2CO_3$ by lowering the conduction band position and meanwhile generating impurity level. The photocatalytic performance is evaluated by monitoring NO removal from the gas phase, photodegradation of a colorless contaminant (bisphenol A, BPA) in an aqueous solution, and photocurrent generation. In comparison with the pristine $Bi_2O_2CO_3$ which is not sensitive to visible light, the self-doped $Bi_2O_2CO_3$ exhibits drastically enhanced visible-light photoreactivity, which is also superior to that of many other well-known photocatalysts such as P25, C_3N_4, and BiOBr. The highly enhanced photocatalytic performance is attributed to combination of both efficient visible light absorption and separation of photogenerated electron−hole pairs. The self-doped $Bi_2O_2CO_3$ also shows decent photochemical stability, which is of especial importance for its practical applications. This work demonstrates that self-doping with an anionic group enables the band gap engineering and the design of high-performance photocatalysts sensitive to visible light.

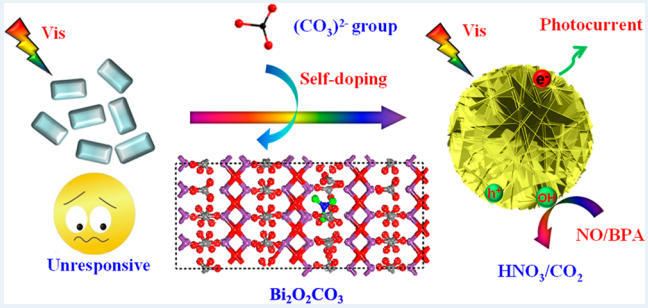

KEYWORDS: *photocatalysis, $Bi_2O_2CO_3$, self-doping, band gap, charge separation*

1. INTRODUCTION

Semiconductor-based photocatalysis, a desirable method for energy generation and contamination management, shows great potentials for CO_2 conversion, hydrogen evolution, NO removal from air, and degradation of organic pollutants.[1−3] To utilize solar energy efficiently, the photocatalysts are required to have a broad photoresponsive range. Various strategies have been developed to tune the band gap of photocatalysts to enhance the absorbance in visible light region.[4−7] Self-doping, a facile and efficient technique arousing considerable interest in semiconductor photocatalysis,[8−11] can boost the light absorption efficacy while the potential adverse impact by doping with extraneous species, for instance, undesirable thermal instability, can be avoided. Self-doping can lead to the narrowed bandgap or formation of intermediate levels between the conduction band (CB) and valence band (VB), thus extending the photosensitive range of a photocatalyst.[10] Based on this route, a wide bandgap photocatalyst can be effectively excited only by absorbing visible photon energy. For example, Ti^{3+} self-doping can extend the absorption range of TiO_2 from the UV to visible light regions, thereby resulting in enhanced visible-light photocatalytic hydrogen-evolution activity.[8] I^- self-doping enables BiOI the tunable band gap via varying the different doping concentrations, and consequently promotes the photocatalysis property under visible light irradiation.[9] Moreover, it has recently been

Received: March 2, 2015
Revised: May 27, 2015
Published: June 3, 2015

DOI: 10.1021/acscatal.5b00444
ACS Catal. 2015, 5, 4094−4103

demonstrated that the Bi^{3+} self-dopant introduces a local impurity level in the band structure of Bi_2WO_6, which is found to be beneficial to electron excitation in photocatalysis process, enhancing the photocatalytic activity.[10] Anionic groups are constituted by various atoms and different compositions. The anionic groups doping may provide more possibilities for modulation and management on the crystal structure, optical properties, optoelectronic properties and photocatalytic activitis of the semiconductors. Nevertheless, most of the self-doping researches have focused on cationic or anionic ions, but self-doping with an anionic group has seldom been explored.

As a typical anionic-group containing Bi-based photocatalyst, bismuth subcarbonate ($Bi_2O_2CO_3$) has the interesting "Sillén" or "Aurivillius" related structure as well as efficient photocatalytic activity.[12−15] Although the large internal electric field and asymmetrical polarization effect may enhance the photocatalytic properties of $Bi_2O_2CO_3$,[16−18] its application to photodegradation is limited by the large band gap of pristine $Bi_2O_2CO_3$ (~3.3 eV). Thus, there have been intensive researches on the morphological modulation,[19,20] fabrication of heterojunctions,[21−30] graphene decoration,[31,32] noble metal deposition,[33] as well as elemental doping.[34−36] In view of the internal $[CO_3]^{2-}$ anionic group and layered configuration suitable for modification, $Bi_2O_2CO_3$ may be a viable substrate to probe the effects of anionic group self-doping on wide bandgap semiconductors.

Herein, we report the self-doping of $Bi_2O_2CO_3$ with the carbonate group fabricated with a one-pot hydrothermal technique. Both the sodium citrate and urea as carbonate sources play critical roles in the formation of self-doped $Bi_2O_2CO_3$. Compared to pristine $Bi_2O_2CO_3$ which is not sensitive to visible light, self-doping could enhance the visible light absorption by tuning its band gap. DFT calculation and systematic characterization are performed to investigate the crystal structure, electronic band structures and photoabsorption. Practical utilization of this catalyst is evaluated by NO removal from the gas phase, bisphenol A (BPA) photodegradation in an aqueous solution, and photocurrent generation. The self-doping effect and the mechanism on visible-light photooxidation have been revealed. This work has paved a new way for doping of semiconductor photocatalyst without relying on extra doping source.

2. EXPERIMENTAL SECTION

2.1. Synthesis of Carbonate Self-Doped $Bi_2O_2CO_3$. Carbonate self-doped $Bi_2O_2CO_3$ (C-BOC) and pristine $Bi_2O_2CO_3$ (BOC) were prepared by a one-pot hydrothermal method. All the raw materials were of analytical grade and used as received. Both sodium citrate and urea as the carbonate species source are critical to the formation of the self-doped $Bi_2O_2CO_3$. The synthesis procedure of C-BOC is as following: First, 1 mmol of $Bi(NO_3)_3{\cdot}5H_2O$, 2 mmol of urea, and a certain amount of sodium citrate were dissolved in 35 mL of deionized water. The mixture was magnetically stirred for 1 h to obtain a homogeneous suspension which was then transferred to a Teflon-lined steel autoclave. The autoclave was slowly heated to 160 °C and maintained at this temperature for 24 h. Afterward, the products were filtrated, washed with distilled water, and dried at 60 °C for 20 h. The samples with molar ratios of sodium citrate to $Bi(NO_3)_3{\cdot}5H_2O$ of 0, 0.5, 1, 1.5, and 2 were denoted as BOC, BOC-1, BOC-2, BOC-3, and BOC-4, respectively.

2.2. Characterization. The phase structure of BOC, BOC-1, BOC-2, BOC-3, and BOC-4 was characterized by X-ray diffraction (XRD) using monochromatic Cu K_α radiation (Bruker, Germany). The morphology and structure were determined by scanning electron microscopy (SEM, S-4800), transmission electron microscopy (TEM) and high-resolution TEM (HR-TEM, JEM-2100 JEOL, Japan). A Bruker spectrometer was used to acquire the Fourier-transform infrared (FTIR) spectra in the frequency range from 500 to 4000 cm^{-1}. Raman scattering in the range between 200 and 1500 cm^{-1} was conducted on the Raman-11 spectrometer. X-ray photoelectron spectroscopy (XPS) was performed on a VGMK II X-ray to determine the chemical composition and chemical states. BET specific surface areas were characterized with the nitrogen adsorption method on the Micromeritics 3020 instrument. UV−vis diffuse reflectance spectra (DRS) were obtained to investigate light absorption and a Hitachi F-4600 fluorescence spectrophotometer was utilized to obtain the photoluminescence (PL) spectra. *In situ* electron paramagnetic resonance (EPR) was performed on the JEOL ES-ED3X Endor spectrometer at 77 K. The spin trapping electron spin resonance (ESR) measurements were performed on a Bruker JES FA200 ESR spectrometer with a xenon lamp as the visible light source. DMPO (5,5′-dimethyl-1-pirroline-N-oxide) was employed as a spin-trap reagent to trap the active species of hydroxyl ($^{\bullet}OH$) and superoxide radicals ($^{\bullet}O_2^-$).

2.3. Photocatalytic Evaluation. The photocatalytic activity is assessed by NO removal from the gas phase (λ > 420 nm, 100 W tungsten halogen lamp) and photodecomposition of colorless bisphenol A (BPA) in an aqueous solution (λ > 420 nm, 500 W xenon lamp) under visible light irradiation.

Degradation of BPA. Fifty milligrams of the photocatalyst were ultrasonically dispersed in 50 mL of the BPA aqueous solution (10 mg/L). Before light irradiation, the suspension was magnetically stirred in darkness for 1 h to achieve an absorption−desorption equilibrium. Afterward, light was turned on. At preselected time intervals, 3 mL of the suspension was sampled and centrifuged to get rid of the solid particles. Finally, the concentration of BPA was determined by colorimetry on a UV-5500PC UV−vis spectrophotometer.

Removal of NO. The 4.5 L (30 cm × 15 cm × 10 cm) organic glass reactor with continuous flow was utilized to remove NO; 0.20 g of the photocatalyst was ultrasonically dispersed in 50 mL of deionized water and coated on a glass dish with a diameter of 12.0 cm. After it was dried, it was put on the reactor center. The concentration of NO was diluted from 100 ppm (N_2 balance) to about 600 ppb by mixing with flowing air. The NO and air stream were premixed using a three-way valve and the flow rates were 15 and 2.4 L min^{-1}, respectively. After equilibrating, the photocatalyst was exposed to visible light. At every min, the concentration of NO was determined by measuring the concentration of NO_2 and NOx (NO_x representing the total concentration of NO + NO_2) using a NOx analyzer (42i-TL, Thermo Scientific). Similar to degradation in the liquid phase, the removal efficiency of NO (η) can be calculated from $(\eta\%) = (1 - C/C_0) \times 100\%$, where C_0 and C are the inlet and outlet concentrations of NO, respectively.

2.4. Photoelectrochemical Measurements. Photoelectrochemical measurements are carried out using a three-electrode quartz cell on the CHI-660B electrochemical system. The saturated calomel electrode (SCE) was the reference electrode, and platinum wire serves as counter electrode. The working electrodes were BOC and C-BOC films coated on ITO and the electrolyte was 0.1 M Na_2SO_4 solution. All the photoelectrochemical measurements are performed under visible light irradiation emitted from a 500 W Xe lamp with 420 nm cutoff filters. The average light power was 45 mW/cm^2.

2.5. Density Functional Theory (DFT) Calculation. To investigate the crystal structure and electronic band structure of self-doped $Bi_2O_2CO_3$, DFT calculation is carried out by utilizing CASETP code implemented plane-wave method and Perdew−Burke−Ernzerhof function.[37,38] In the Brillouin zone integration, a Monkhorst−Pack k-point mesh of 2 × 1 × 2 is adopted, and the energy cutoff is chosen as 400 eV.

3. RESULTS AND DISCUSSION

3.1. Crystal Structures, Morphology, and Formation Mechanism of CO_3^{2-}-Doped $Bi_2O_2CO_3$. Figure 1 depicts the

DOI: 10.1021/acscatal.5b00444
ACS Catal. 2015, 5, 4094−4103

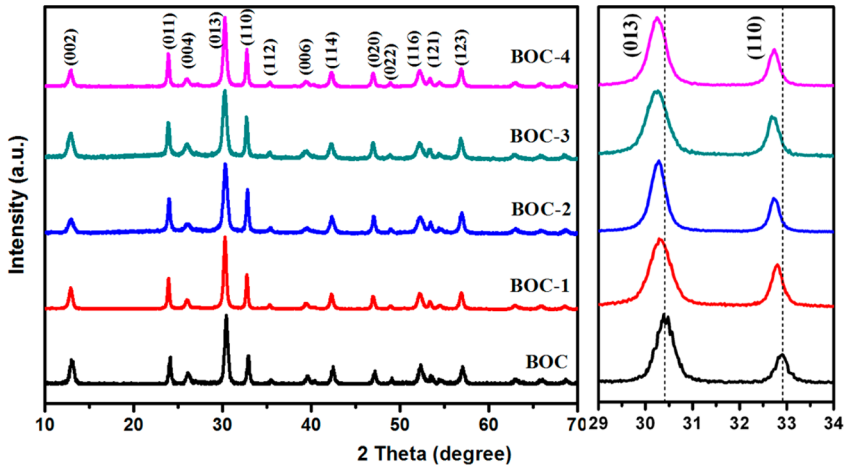

Figure 1. XRD patterns of BOC, BOC-1, BOC-2, BOC-3, and BOC-4.

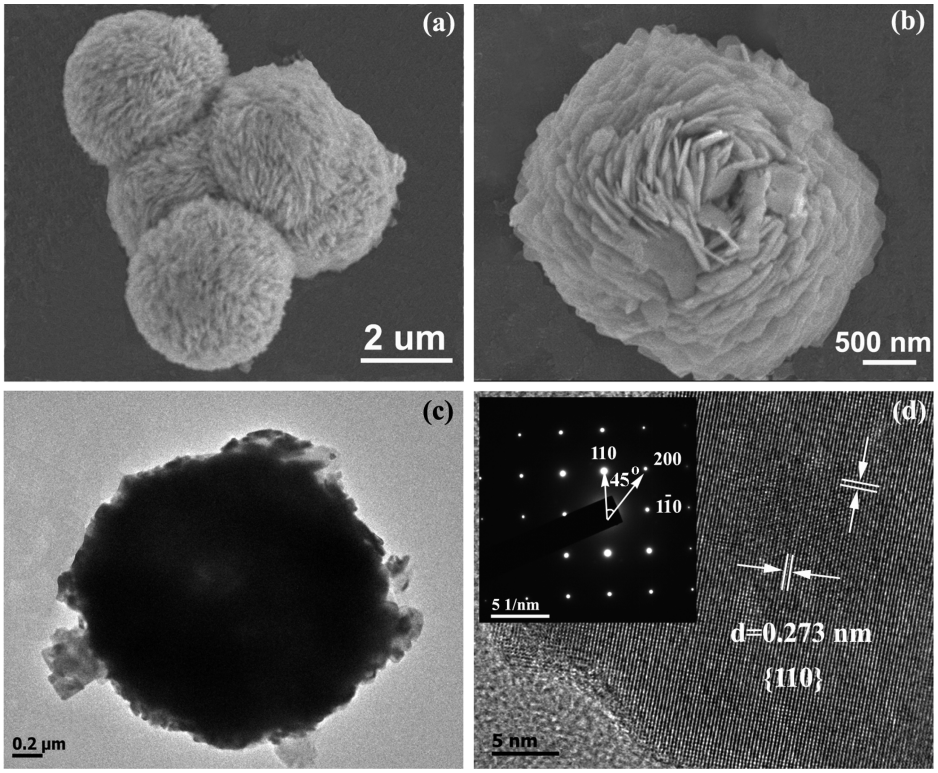

Figure 2. (a, b) SEM images and (c, d) TEM and SAED images (inset) of C-BOC (BOC-3).

X-ray diffraction (XRD) patterns of the pristine $Bi_2O_2CO_3$ (BOC) and carbonate self-doped $Bi_2O_2CO_3$ (C-BOC) samples. All the diffraction peaks can be indexed to the tetragonal phase of $Bi_2O_2CO_3$ (JCPDS Card No. 41-1488), indicating the pure phase of samples and that the dopant does not change the preferential orientation and crystalline phase of the $Bi_2O_2CO_3$. Nevertheless, according to the enlarged pattern, the peaks assigned to (110) and (013) shift gradually to smaller angles with increasing dopant concentration. According to Bragg's law ($n\lambda = 2d \sin \theta$), a smaller 2θ value indicates a larger lattice spacing.[39] XRD result implies that some dopants are actually incorporated into the crystalline lattice of $Bi_2O_2CO_3$ enlarging the unit cell parameters.

The Fourier transform infrared (FTIR) spectra of BOC and C-BOC are presented in Figure S1. The two intense peaks at 1392 and 1468 cm^{-1} are assigned to the antisymmetrical stretching vibration mode of the CO_3^{2-} group and the sharp peak at 843 cm^{-1} corresponds to the bending mode of the CO_3^{2-} group.[34] The intensities of all the CO_3^{2-} characteristic vibration bands of C-BOC samples increase gradually with increasing the amount of sodium citrate (from BOC to BOC-4), especially for the antisymmetrical stretching vibration at 1468 cm^{-1}. This result demonstrates that sodium citrate can act as carbonate source and release CO_3^{2-} anionic group, which is then incorporated into the crystal structure of $Bi_2O_2CO_3$.

The morphology of the samples is investigated by SEM. The concentration of sodium citrate can largely affect the morphology of the $Bi_2O_2CO_3$.[19,20] In contrast to the pristine BOC composed of a large amount of single nanoplates (Figure S2a), the morphology of doped $Bi_2O_2CO_3$ gradually transforms

DOI: 10.1021/acscatal.5b00444
ACS Catal. 2015, 5, 4094−4103

from two-dimensional (2D) nanoplates to hierarchical 3D microspherical architectures with increasing the amount of sodium citrate (Figure S2). BOC-3 and BOC-4 exhibit uniform microsphere structure with a diameter of 2−2.5 μm constructed by nanosheets (Figure 2a and b and Figure S2d). This morphology is expected to enhance light harvest due to multiple scattering and reflection. The surface areas of the samples are measured to be 9.6, 12.5, 15.7, 18.2, and 18.7 cm^2/g for the pristine $Bi_2O_2CO_3$, BOC-1, BOC-2, BOC-3, and BOC-4, respectively. The surface areas gradually increase with increasing the sodium citrate amount and almost keep unchanged with further raising sodium citrate amount (BOC-4). Figure 2c confirms the microspherical structure of C-BOC. The HR-TEM image (Figure 2d) reveals two sets of lattice fringes with a lattice spacing of 0.273 nm corresponding to the {110} facet of orthorhombic $Bi_2O_2CO_3$. A clear square diffraction spot array indicating high crystallinity is observed from the corresponding selected-area electron diffraction (SAED) pattern (inset in Figure 2d). The labeled angle in this pattern is 45°, which is in accordance with the value between the {110} and {200} facets.

On the basis of the above experimental results, a plausible two-step growth mechanism for the formation process of CO_3^{2-}-doped $Bi_2O_2CO_3$ is proposed, as shown in Scheme 1.

Scheme 1. Schematic Illustration of the Possible Formation Process of the C-BOC Hierarchical Microsphere[a]

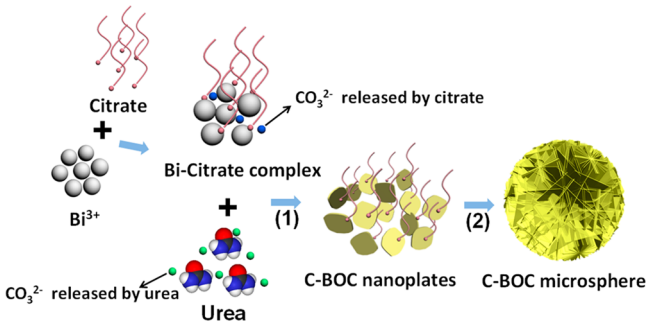

[a](1) Formation of C-BOC nanoplates; (2) citrate-induced self-assembly of these primary nanoplates to form regular hierarchical microsphere.

Both the sodium citrate and urea are considered to play crucial roles in the formation process of self-doped $Bi_2O_2CO_3$. Urea can provide adequate amount of CO_3^{2-} ions for formation of pristine $Bi_2O_2CO_3$. As a complexing agent with three carboxylic groups and a hydroxyl group, sodium citrate plays a significant role in releasing doped CO_3^{2-} ions as well as the growth of such $Bi_2O_2CO_3$ hierarchical microspheres.[19,20] Maybe the sodium citrate is easier to release doped CO_3^{2-} ion in a favorable chemical environment created by large amount of urea. They may comaintain a favorable environment more suitable for CO_3^{2-} ion doping. In the first step, bicitrate complexes are formed via an electrostatic interaction between the Bi^{3+} ion and the citrate. This action is beneficial to impede the hydrolysis of Bi^{3+} ion and promote its dispersion in the aqueous system. In the following hydrothermal process, these Bicitrate complexes reacted with CO_3^{2-} ions released by urea to form the $Bi_2O_2CO_3$ nanoplates. During this process, citrate serves as a capping reagent, separating the crystal nucleus and limiting the further growth of the nanoplates. On the other hand, more CO_3^{2-} ions are released by decomposition of citrate and then incorporated into the crystal structure of $Bi_2O_2CO_3$ nanoplates. The hierarchical microspheres of CO_3^{2-}-doped $Bi_2O_2CO_3$ are formed in the second step. The free citrate attaches on the surfaces of firstborn $Bi_2O_2CO_3$ nanoplates and directs their self-assembly, inducing the final formation of CO_3^{2-}-doped hierarchical microspheres.

3.2. Chemical Coordination, Oxygen Vacancy, and Thermogravimetric Analysis. To obtain more information about the dopant and chemical coordination of each atom, X-ray photoelectron spectroscopy (XPS) is conducted on BOC and C-BOC. As shown in Figure 3a, Bi, O, and C can be detected from both samples whereas an intensive C peak is observed from C-BOC. The high-resolution C 1s spectra (Figure 3b) show two peaks with binding energies of 284.8 and 288.4 eV. The former is attributed to the adventitious carbon (AC) from the instrument and the latter corresponds to carbonate. Compared to BOC, a more intensive peak at 288.4 eV is observed from C-BOC indicating a larger amount of carbonate. Significantly, different from the carbon-doped $Bi_2O_2CO_3$ which shows a Bi−C bond band at 283.05 eV, the absence of the Bi−C peak in our doped $Bi_2O_2CO_3$ excludes the carbon doping or formation of bismuth carbide.[36] The two peaks at 164.73 and 159.47 eV in BOC are associated with Bi $4f_{5/2}$ and Bi $4f_{7/2}$, respectively (Figure 3c).[40] The shift of the two characteristic peaks of C-BOC to lower binding energy may be ascribed to the change in the chemical coordination of Bi^{3+}. The O 1s spectra (Figure 3d) can be deconvoluted into three peaks at 531.7, 530.9, and 530.0 eV, which can be assigned to the surface hydroxyl groups, carbonate species, and characteristic of Bi−O in $Bi_2O_2CO_3$, respectively.[34,41] In comparison with BOC, the C-BOC exhibits a stronger C−O intensity implying a larger carbonate concentration. Both the C 1s and O 1s XPS spectra furnish the direct evidence of successful fabrication of carbonate self-doped $Bi_2O_2CO_3$. The doped carbonate species is expected to introduce intermediate levels in the forbidden band to narrow the band gap of $Bi_2O_2CO_3$. The doping of carbonate species has been achieved without extra doping source, which is different from previous doping methods.

The introduction of dopant into matrix always leads to the presence of crystal defect, which can be probed by in situ electron paramagnetic resonance (EPR) technique. As shown in Figure S3, no signals were generated over BOC sample. In contrast to the case of BOC, the C-BOC presents a distinct signal peak at $g \approx 2.001$ by taking manganese signal as reference. This peak is considered to be the characteristic of surface oxygen vacancy.[42,43] Though the surface oxygen vacancy may only slightly improve the photoabsorption of a crystal,[43] it can serve as traps for photoinduced charge to inhibit the hole−electron recombination, thereby promoting the photocatalytic process.[44]

Thermogravimetric (TG) analysis is employed to quantificationally determine the CO_3^{2-} self-doping amount of the samples, as $Bi_2O_2CO_3$ can decompose to Bi_2O_3 and CO_2 at certain temperature. TG curves of BOC, BOC-1 and BOC-3 (Figure 4) are measured to investigate the doped CO_3^{2-} amount. The TG results reveal that they all exhibit weight loss in the temperature range of 260−330 °C and the weight loss of pristine $Bi_2O_2CO_3$ is 8.6%, which is in good agreement with the CO_2 loss (8.63%) of pristine $Bi_2O_2CO_3$. The weight losses of BOC-1 and BOC-3 are 9.8% and 10.7%, respectively, corresponding to the CO_3^{2-} self-doping concentration of 13.9% and 24.4%, respectively. The TG results further confirm the

DOI: 10.1021/acscatal.5b00444
ACS Catal. 2015, 5, 4094−4103

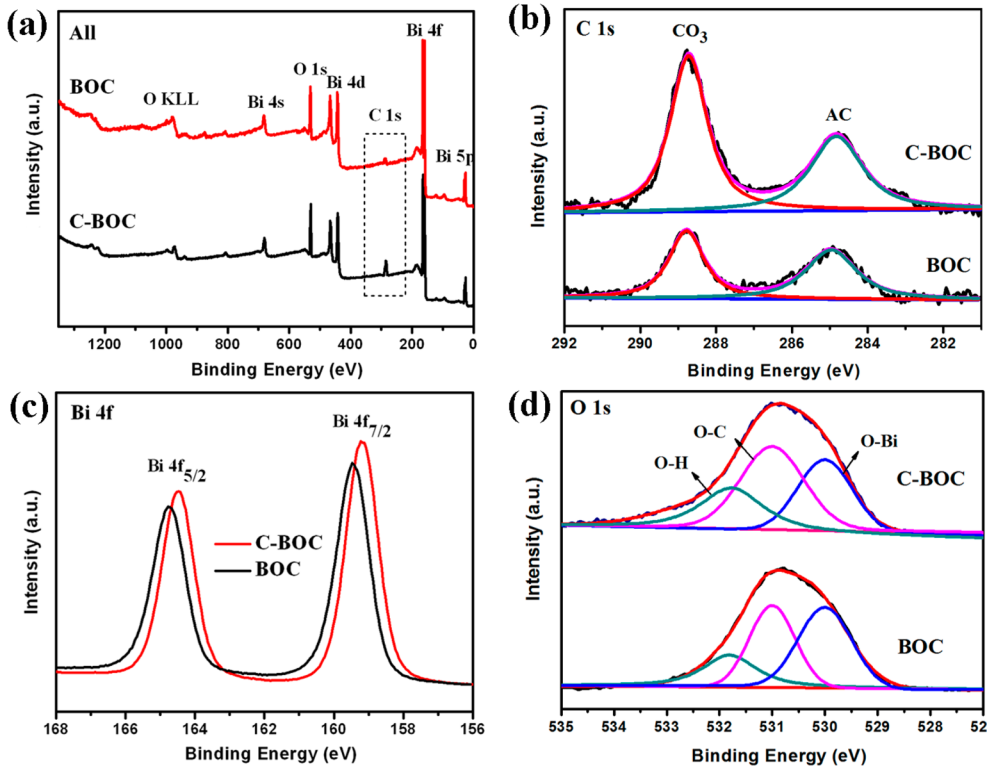

Figure 3. (a) Survey XPS spectra and high-resolution XPS spectra of (b) C 1s, (c) Bi 4f, and (d) O 1s.

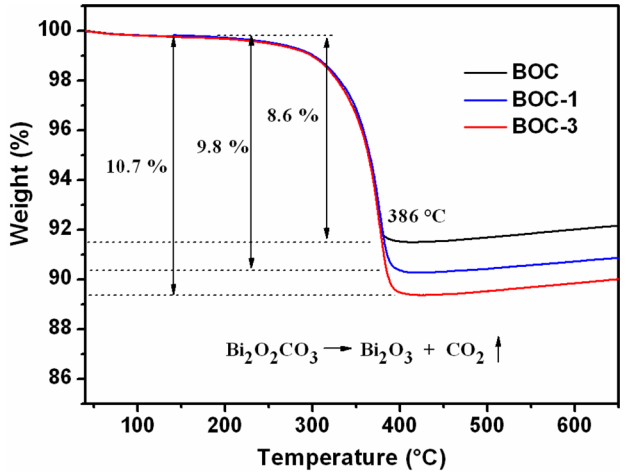

Figure 4. TG curves of BOC, BOC-1, and BOC-3.

CO_3^{2-} self-doping and give a quantitative analysis on CO_3^{2-} dopant.

3.3. Optical Properties and Tunable Bandgap. UV−vis diffuse reflection spectra (DRS) are acquired to determine the optical properties of the samples. Figure 5a displays the DRS of the pristine BOC and C-BOC. C-BOC shows more absorption in the UV region than the pristine $Bi_2O_2CO_3$ on account of the hierarchical microstructure. All the doped samples exhibit absorption in the visible region because the incorporated carbonate extends the light absorption range of BOC from the UV to visible region. It can also be found that light absorption is continuously enhanced from BOC-1 to BOC-4. This should be attributed to the continuously increased CO_3^{2-} self-doping amount and light trapping effect derived from the 3D microspherical architectures. The corresponding color change in the products is displayed in the inset in Figure 5b. Significantly different from the dark gray or black colors of carbon-doped $Bi_2O_2CO_3$ (Figure S4)[36] and other carbon-doped photocatalysts,[45,46] all the C-BOC samples obtained here are yellow, which provides indirect evidence that carbon doping can be excluded.

The band gap of BOC can be obtained by the Kubelka−Munk (KM) expression:[47]

$$\alpha h\nu = A(h\nu - E_g)^{n/2} \quad (1)$$

where A, $h\nu$, E_g, and α are the proportionality constant, photonic energy, band gap, and optical absorption coefficient, respectively. The band gaps of BOC, BOC-1, BOC-2, BOC-3, and BOC-4 are calculated to be 3.25, 3.06, 2.97, 2.81, and 2.72 eV, respectively (inset in Figure 5a). The band gap can be tuned from 3.25 to 2.72 eV by varying the precursor molar ratio from 0 to 2. The band gap narrows gradually with dopant amount, as shown in Figure 5b.

3.4. Investigations on Band Structures by the Theoretical Calculations and Experimental Methods. Density functional theory (DFT) calculation is used to investigate the crystal and electronic structure of CO_3^{2-} self-doped $Bi_2O_2CO_3$. The result from crystal structure optimizing indicates that the foreign CO_3^{2-} ions are doped in the caves constructed by the four adjacent CO_3^{2-} ions, as shown in Figure 6a and Figure S5. The valence band (VB) and conduction band (CB) structures of pure and self-doped $Bi_2O_2CO_3$ are depicted in Figure 6b. The denser band density of self-doped BOC is resulted from its 2 × 1 × 2 super cell. Compared to the pristine $Bi_2O_2CO_3$ with a band gap of 3.10 eV, the self-doped CO_3^{2-} ions effectively narrow the band gap of $Bi_2O_2CO_3$ (2.42 eV) by lowering the CB position for ∼0.68 eV, which is consistent with the results obtained from the UV−vis diffuse reflection spectra. Meanwhile, it is interesting to

DOI: 10.1021/acscatal.5b00444
ACS Catal. 2015, 5, 4094−4103

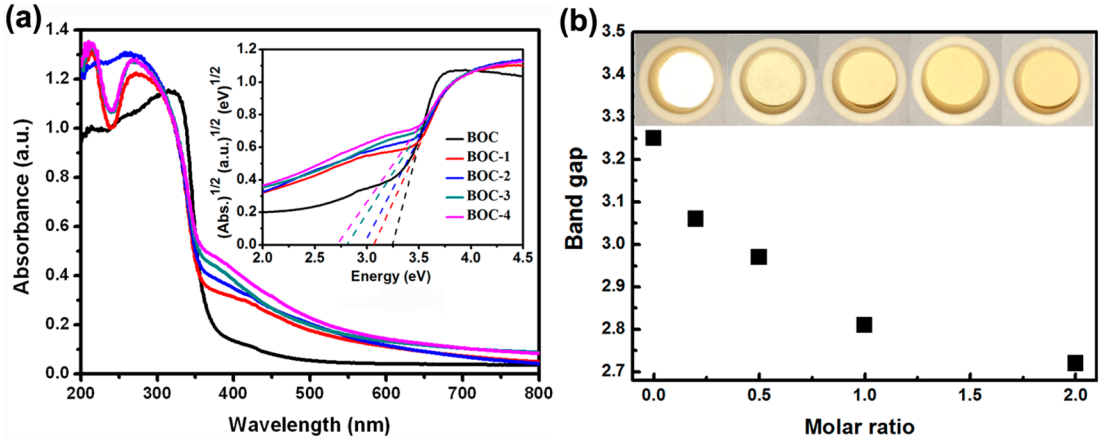

Figure 5. (a) UV−vis diffuse reflectance spectra and bandgap energies (inset of a); (b) Plot of band gap versus precursor molar ratio (sodium citrate to $Bi(NO_3)_3{\cdot}5H_2O$) and corresponding color (inset of b) of BOC, BOC-1, BOC-2, BOC-3, and BOC-4.

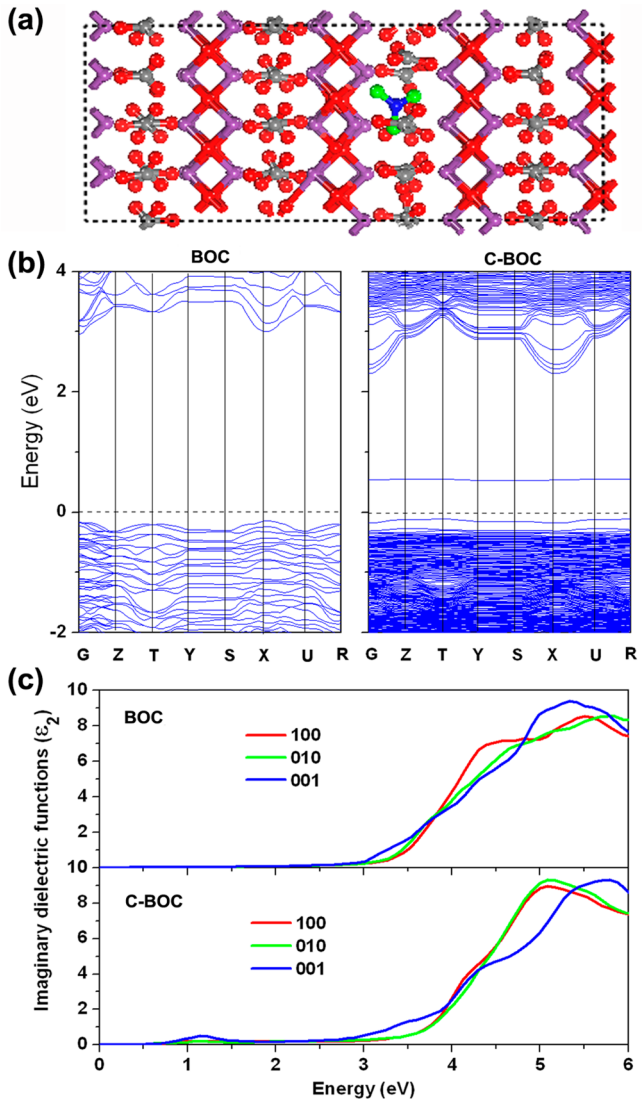

Figure 6. (a) Crystal structure of C-BOC. (b) Electronic band structures of BOC and C-BOC. (c) Calculated imaginary dielectric functions versus energy of BOC and C-BOC.

notice that an impurity level composed of O 2p orbital (Figure S6) are generated above the Fermi level, which accords well with the characteristic of doping. It is expected that this modified band structure is beneficial to electron excitation in photocatalysis process.[10]

Imaginary dielectric functions of BOC and C-BOC along three crystallographic axes are displayed in Figure 6c.[48] The pristine BOC can only absorb light with energy larger than 3.1 eV, which agrees with its electronic band structure and DRS. Comparatively, the photoresponse of C-BOC is extended to 2.0 eV and meanwhile an obvious absorption band at 1.2 eV appears, confirming the narrowed band gap and generation of impurity level. Additionally, it is also observed that the more absorbance in high-energy area results from light trapping effect of 3D microspherical architectures of C-BOC, matching well with the DRS results.

To further corroborate the theoretical calculation results and the band structure evolution of CO_3^{2-} self-doped $Bi_2O_2CO_3$ experimentally, the VB XPS and Mott−Schottky curves of BOC and C-BOC are measured. As shown in Figure 7a, the C-BOC exhibits a similar VB edge in comparison with that of BOC, indicating that the VB position of C-BOC is almost not changed compared to that of BOC. Figure 7b displays the Mott−Schottky curves of the two samples, which can be used to determine the flat potentials of semiconductors.[49] The positive slope of linear $1/C^2$ potential curves disclose the characteristic of n-type semiconductor of $Bi_2O_2CO_3$. Compared with the pure BOC, the flat potential of C-BOC is lowered by 0.42 eV, which accords with the decrease of band gap from 3.25 to 2.81 eV. As the CB potentials of n-type semiconductors are slightly higher (~0.1−0.3 eV) than the flat potentials, it can be concluded that the CB position of C-BOC is lowered in comparison with that of BOC. The VB XPS and Mott−Schottky curve measurements are consistent with the DFT calculation results, further confirming the role of the CO_3^{2-} self-doping in tuning the band gap.

3.5. Visible-Light-Sensitive Photocatalytic Reactivity, Photoelectrochemical Properties, and Mechanism. The photocatalytic activity of BOC and C-BOC is assessed by studying NO removal from the gas phase and photodecomposition of colorless BPA in an aqueous solution under visible light illumination (λ > 420 nm). As shown in Figure 8a, compared to pure BOC which does not absorb visible light, all the C-BOC samples exhibit visible-light-driven photocatalytic activity for BPA degradation, and the degradation efficiency of self-doped BOC first gradually increases and then decreases

DOI: 10.1021/acscatal.5b00444
ACS Catal. 2015, 5, 4094−4103

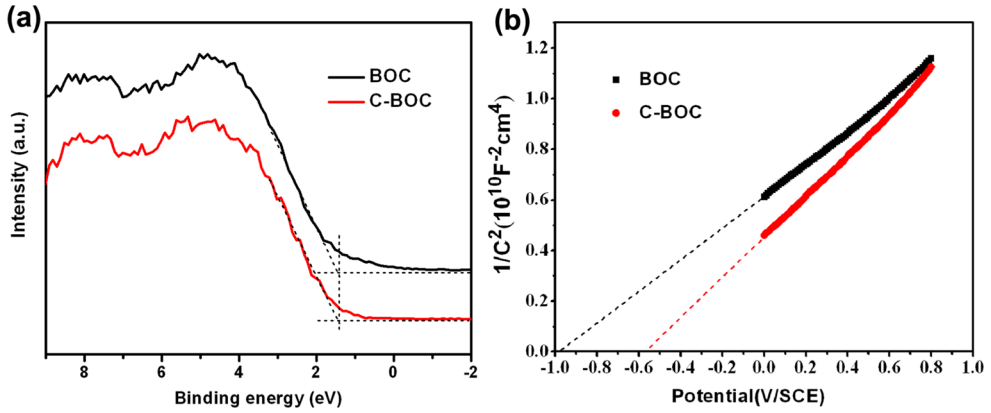

Figure 7. (a) VB XPS and (b) Mott–Schottky curves of BOC and C-BiOC (BOC-3).

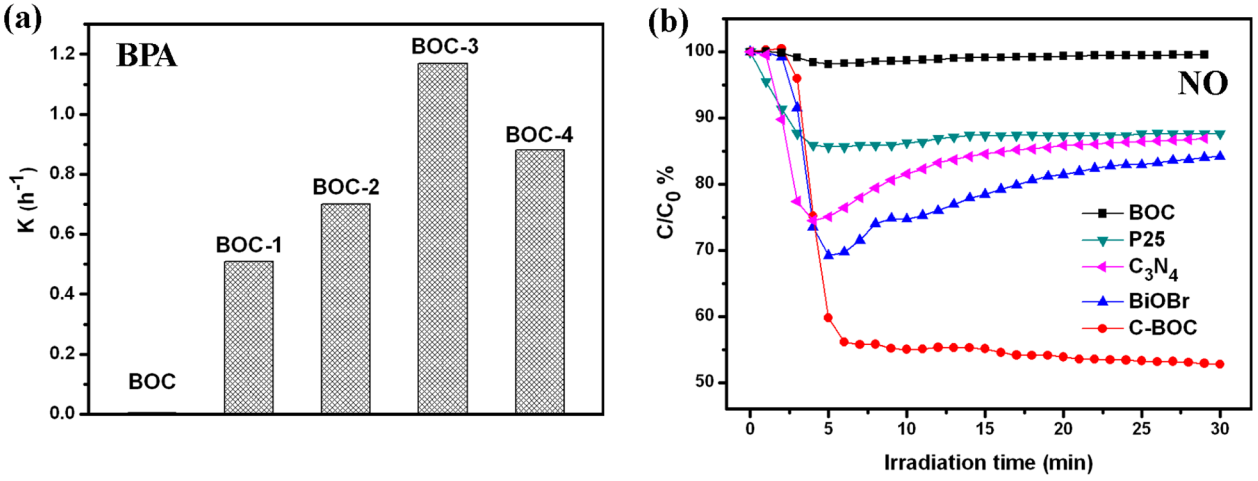

Figure 8. (a) Apparent rate constants for degradation of BPA by BOC, BOC-1, BOC-2, BOC-3, and BOC-4; (b) NO removal curves of BOC, C-BOC (BOC-3), P25, C_3N_4, and BiOBr under irradiation of visible light (λ > 420 nm).

(observed for BOC-4) with increasing the CO_3^{2-} doping amount. The enhancement on photocatalytic activity may be attributed to the gradually enhanced light absorbance and specific surface areas. Nevertheless, excessive dopants might result in the formation of recombination centers of photogenerated electron and holes, detrimental to photocatalytic activity.[50] Thus, BOC-3 shows the highest photodegradation efficiency with an apparent rate constant 1.17 h^{-1}. To compare the enhancement degree of photoactivity quantitatively, simulated solar light is also used as light source. The BOC-3 exhibits a significantly enhanced photodegradation rate under UV–vis light irradiation, approximately 11.3 time that of pristine BOC (Figure S7). Furthermore, NO removal is monitored to evaluate the photocatalytic performance under visible light as NO can be oxidized by photoinduced active species to produce HNO_3 as the final product. Figure 8b displays the changes in the NO concentration versus irradiation time. NO removal observed from the pristine BOC is negligible but C-BOC shows an efficient removal ratio of 48%, which is also far superior to those of other well-known photocatalysts that used to effectively remove NO, such as P25 (12%), C_3N_4 (13%) and BiOBr (16%).

The interfacial charge separation and transfer dynamics of photoelectrons are studied by monitoring the photocurrent–time response that is correlated with the photocatalytic activity.[51] Figure 9a shows the photocurrent response of the BOC and C-BOC electrodes under illumination of visible light (λ > 420 nm). There is no photocurrent on BOC regardless of whether there is light or not. On the other hand, C-BOC shows a rapid and dramatic photocurrent generation with good reproducibility during visible light illumination revealing the generation of photoexcited electrons. The results demonstrate effective separation of photoinduced electron–hole pairs in C-BOC upon exposure to visible light.

Electrochemical impedance spectroscopy (EIS) is employed to monitor the charge migration process on the electrodes.[47,52] Generally, a higher charge mobility results in a smaller EIS arc radius. Figure 9b shows the EIS Nyquist plots of the BOC and C-BOC electrodes. The arc radius of C-BOC is much smaller than that of pristine BOC, demonstrating that the carbonate dopant has a positive effect on the separation and transfer efficiency of photogenerated electron–hole pairs. The lifetime (τ) of the injected electrons can be determined by the following expression:[53,54]

$$\tau = 1/2\pi f \qquad (2)$$

where f indicates the inverse minimum frequency. As indicated by the Bode-phase spectra in Figure 9c, the electron lifetimes of BOC and C-BOC are calculated to be 25.9 and 54.7 μs, respectively. The greatly prolonged electron lifetime of C-BOC indicates that self-doping with CO_3^{2-} promotes the separation and migration of electron–hole pairs in $Bi_2O_2CO_3$.

DOI: 10.1021/acscatal.5b00444
ACS Catal. 2015, 5, 4094–4103

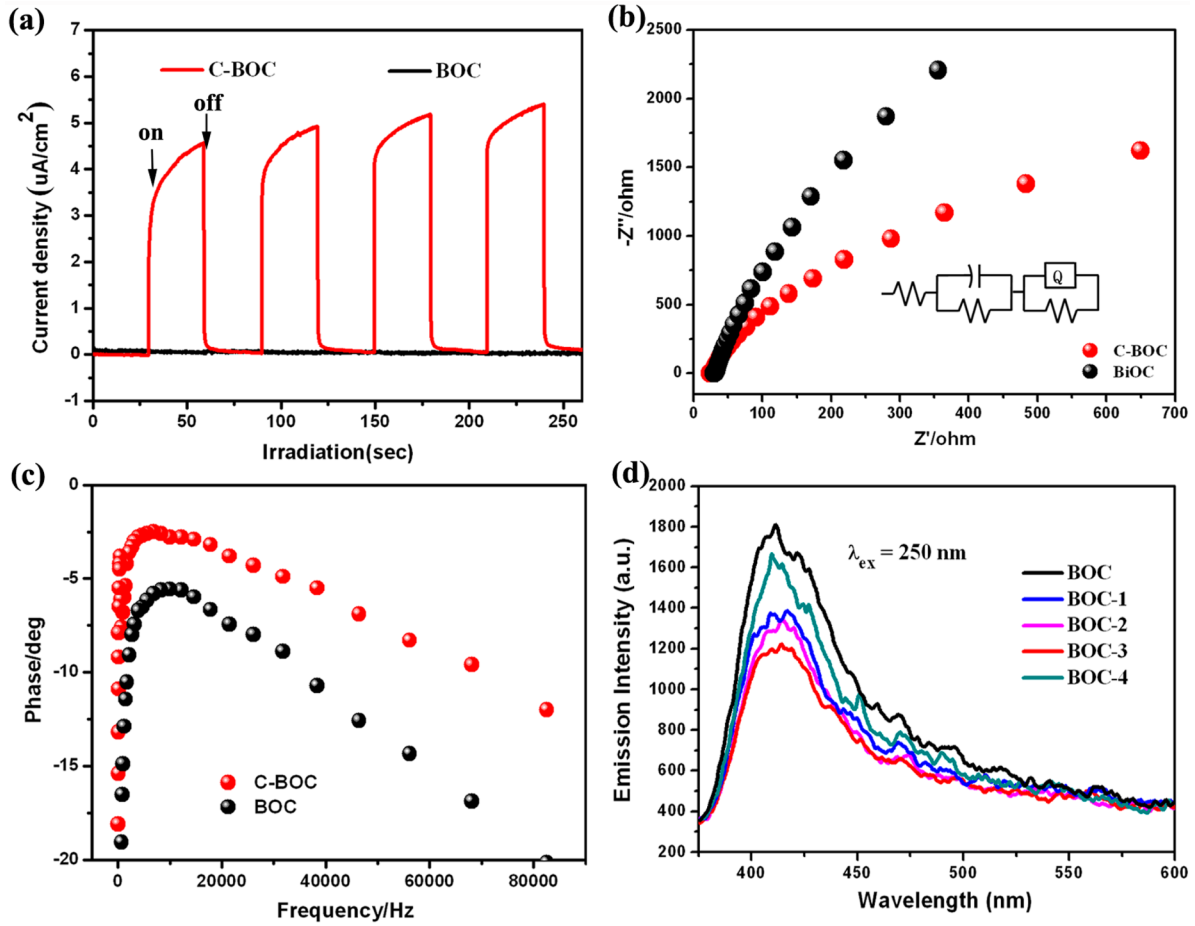

Figure 9. (a) Transient photocurrent densities, (b) EIS Nyquist plots, and (c) Bode-phase spectra of BOC and C-BOC (BOC-3) under visible light irradiation (λ > 420 nm). (d) PL spectra of BOC, BOC-1, BOC-2, BOC-3, and BOC-4 excited by 250 nm.

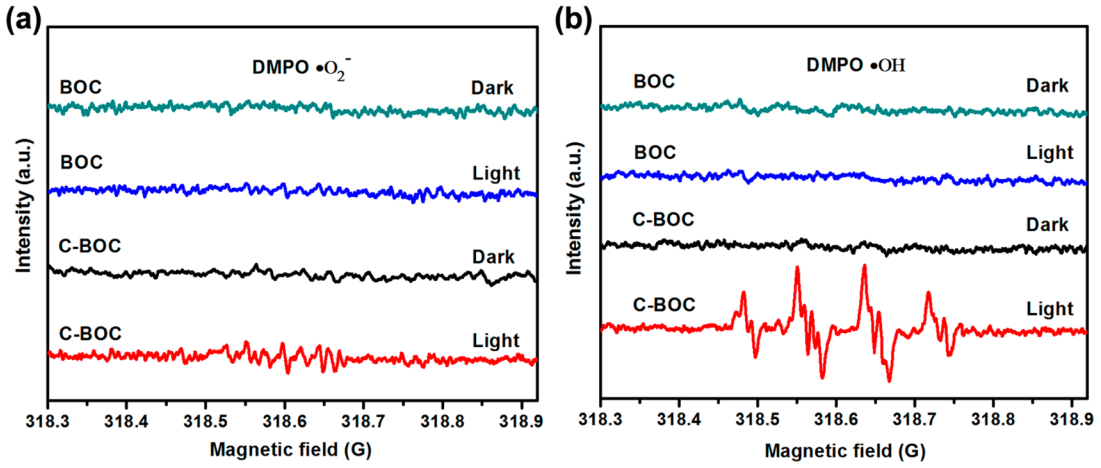

Figure 10. ESR spectra of (a) DMPO−$^{\bullet}O_2^-$ and (b) DMPO−$^{\bullet}$OH adducts of BOC and C-BOC samples in darkness and under visible light irradiation.

Photoluminescence (PL) is performed to confirm the enhanced separation efficiency of photogenerated charge carriers in C-BOC.[55] As shown in Figure 9d, all the doped samples display lower PL emission than the pristine BOC, indicating that recombination emission by bulk and surface traps is reduced by carbonate self-doping. The largest PL reduction is observed from BOC-3 indicative of the smallest recombination rate of photogenerated electrons and holes at this optimal doping concentration. This confirms that an excessive dopant amount could lead to the formation of surface recombination centers that increase the recombination rate of electrons and holes as revealed by the high PL emission intensity observed from BOC-4.[50] PL verifies the enhanced separation rate of electron−hole pairs by carbonate self-doping and that the photocatalytic performance can be optimized by the doping amount.

DOI: 10.1021/acscatal.5b00444
ACS Catal. 2015, 5, 4094−4103

On the basis of the above analysis, there are two main reasons for the efficient visible-light photocatalytic activity of C-BOC. First, self-doping of carbonate species lowers the CB position and introduces intermediate levels into the forbidden band to narrow the bandgap, thereby expanding the response range of $Bi_2O_2CO_3$ and improving visible light absorption. Second, carbonate self-doping also introduces surface oxygen vacancy to the $Bi_2O_2CO_3$ crystal to facilitate charge transfer and reduce recombination of charge carriers to promote the photocatalytic process. The synergistic effects of the above two factors give rise to the high performance of self-doped $Bi_2O_2CO_3$ under visible light illumination. To monitor the active radicals and determine the photoreaction mechanism, electron spin resonance (ESR) spin-trap technique is employed during irradiation. DMPO (5,5-dimethyl-1-pyrroline N-oxide), a nitrone spin trapping reagent, is utilized to capture the superoxide ($^{\bullet}O_2^-$) and hydroxyl radicals ($^{\bullet}OH$).[10,56] As shown in Figure 10a and b, no ESR signals can be detected from BOC with or without light irradiation. With respect to the ESR signals of DMPO−$^{\bullet}O_2^-$ for C-BOC, the peaks of the DMPO−$^{\bullet}O_2^-$ adducts can be neglected. This demonstrates that O_2 was not reduced to $^{\bullet}O_2^-$ radicals by the photogenerated electrons of C-BOC. In the case of the ESR spectra of DMPO−$^{\bullet}OH$ for C-BOC, four sets of antisymmetric peaks with intensities of 1:2:2:1 are observed, which are the characteristic signals of the DMPO−$^{\bullet}OH$ adducts. ESR demonstrates that $^{\bullet}OH$ radicals are the main active species of C-BOC in the photooxidation process under visible light illumination.

In addition to high photocatalytic activity, the photochemical stability and reproducibility are important factors in commercial applications. The stability and durability of C-BOC are assessed by performing recycling experiments and as shown in Figure S8, no obvious loss in the activity can be observed after five cycles. XRD patterns further confirm the result. As shown in Figure S9, there is no change in the XRD patterns before and after irradiation, implying that the self-doped $Bi_2O_2CO_3$ is stable and not corroded.

4. CONCLUSIONS

Carbonate self-doped $Bi_2O_2CO_3$ with superior visible-light photocatalytic activity is fabricated by a one-pot hydrothermal approach without using additional doping source. The incorporation of CO_3^{2-} into the crystal lattice is verified by both the experimental and theoretical results. The photoresponse range of $Bi_2O_2CO_3$ can be tuned from UV to visible light by self-doping. DFT calculation results disclose that the self-doping herein is interstitial doping and the narrowed band gap is realized by lowering the CB position and generation of impurity level, which is corroborated by VB XPS and Mott−Schottky curves. The self-doped $Bi_2O_2CO_3$ shows highly enhanced visible-light induced NO removal, BPA degradation, and photocurrent response, in contrast to the pristine $Bi_2O_2CO_3$ with no visible light sensitivity. The carbonate dopant and surface oxygen defect are responsible for the high visible-light activity of self-doped $Bi_2O_2CO_3$ as confirmed by in situ EPR, PL, EIS, and Bode-phase spectra. DMPO spin-trapping ESR reveals that more reactive radical species are generated on the self-doped $Bi_2O_2CO_3$ thus accounting for the high visible-light photochemical performance. These findings not only first evidence that self-doping with an anionic group can alter the optical band structure, but also suggest a new direction to the design and fabrication of high-performance visible-light photocatalysts.

■ ASSOCIATED CONTENT

Supporting Information

The Supporting Information is available free of charge on the ACS Publications website at DOI: 10.1021/acscatal.5b00444.

FTIR spectra and SEM images of BOC and C-BOC samples, in situ EPR spectra of BOC and C-BOC, the first-order kinetics photodegradation curves of BPA by BOC and BOC-3, recycling test of BPA degradation, XRD patterns of BOC-3 before and after irradiation, crystal structure and PDOS of C-BOC, and digital photo of carbon-doped $Bi_2O_2CO_3$. (PDF)

■ AUTHOR INFORMATION

Corresponding Authors

*Tel.: +86-10-82322247. E-mail: hhw@cugb.edu.cn.
*E-mail: dfctbu@126.com.
*E-mail: zyh@cugb.edu.cn.

Notes

The authors declare no competing financial interest.

■ ACKNOWLEDGMENTS

This work was jointly supported by the National Natural Science Foundations of China (Grants 51302251, 51322213, 51172245, and 51478070), Fundamental Research Funds for the Central Universities (2652013052), City University of Hong Kong Applied Research Grant (SRG) No. 9667085, and Guangdong−Hong Kong Technology Cooperation Funding Scheme (TCFS) No. GHP/015/12SZ.

■ REFERENCES

(1) Wang, H. L.; Zhang, L. S.; Chen, Z. G.; Hu, J. Q.; Li, S. J.; Wang, Z. H.; Liu, J. S.; Wang, X. C. *Chem. Soc. Rev.* **2014**, *43*, 5234−5244.
(2) Yu, J. G.; Low, J. X.; Xiao, W.; Zhou, P.; Jaroniec, M. *J. Am. Chem. Soc.* **2014**, *136*, 8839−8842.
(3) Shang, L.; Bian, T.; Zhang, B.; Zhang, D. H.; Wu, L. Z.; Tung, C. H.; Yin, Y. D.; Zhang, T. R. *Angew. Chem., Int. Ed.* **2014**, *53*, 250−254.
(4) Linic, S.; Christopher, P.; Ingram, D. B. *Nat. Mater.* **2011**, *10*, 911−921.
(5) Liu, G.; Yang, H. G.; Wang, X. W.; Cheng, L. N.; Pan, J.; Lu, G. Q.; Cheng, H. M. *J. Am. Chem. Soc.* **2009**, *131*, 12868−12869.
(6) Wang, G.; Huang, B. B.; Ma, X. C.; Wang, Z. Y.; Qin, X. Y.; Zhang, X. Y.; Dai, Y.; Whangbo, M.-H. *Angew. Chem., Int. Ed.* **2013**, *52*, 4810−4813.
(7) Feng, N. D.; Wang, Q.; Zheng, A. M.; Zhang, Z. F.; Fan, J.; Liu, S. B.; Amoureux, J. P.; Deng, F. *J. Am. Chem. Soc.* **2013**, *135*, 1607−1616.
(8) Zuo, F.; Wang, L.; Wu, T.; Zhang, Z. Y.; Borchardt, D.; Feng, P. Y. *J. Am. Chem. Soc.* **2010**, *132*, 11856−11857.
(9) Zhang, X.; Zhang, L. Z. *J. Phys. Chem. C* **2010**, *114*, 18198−18206.
(10) Ding, X.; Zhao, K.; Zhang, L. Z. *Environ. Sci. Technol.* **2014**, *48*, 5823−5831.
(11) Dong, G. H.; Zhao, K.; Zhang, L. Z. *Chem. Commun.* **2012**, *48*, 6178−6180.
(12) Chen, R.; So, M. H.; Yang, J.; Deng, F.; Che, C. M.; Sun, H. Z. *Chem. Commun.* **2006**, 2265−2267.
(13) Zheng, Y.; Duan, F.; Chen, M. Q.; Xie, Y. *J. Mol. Catal. A: Chem.* **2010**, *317*, 34−40.
(14) Dong, F.; Ho, W. K.; Lee, S. C.; Wu, Z. B.; Fu, M.; Zou, S. C.; Huang, Y. *J. Mater. Chem.* **2011**, *21*, 12428−12436.
(15) He, R. A.; Cao, S. W.; Zhou, P.; Yu, J. G. *Chin. J. Catal.* **2014**, *35*, 989−1007.

DOI: 10.1021/acscatal.5b00444
ACS Catal. 2015, 5, 4094−4103

(16) Huang, H. W.; Wang, J. J.; Dong, F.; Guo, Y. X.; Tian, N.; Zhang, Y. H.; Zhang, T. R. *Cryst. Growth Des.* **2015**, *15*, 534−537.
(17) Huang, H. W.; Tian, N.; Jin, S. F.; Zhang, Y. H.; Wang, S. B. *Solid State Sci.* **2014**, *30*, 1−5.
(18) Fan, X. Y.; Zang, L.; Zhang, M.; Qiu, H. S.; Wang, Z.; Yin, J.; Jia, H. Z.; Pan, S. L.; Wang, C. Y. *Chem. Mater.* **2014**, *26*, 3169−3174.
(19) Zhao, T. Y.; Zai, J. T.; Xu, M.; Zou, Q.; Su, Y. Z.; Wang, K. X.; Qian, X. F. *CrystEngComm* **2011**, *13*, 4010−4017.
(20) Liu, S. Q.; Tu, Y. Q.; Dai, G. P. *Ceram. Int.* **2014**, *40*, 2343−2348.
(21) Madhusudan, P.; Ran, J. R.; Zhang, J.; Yu, J. G.; Liu, G. *Appl. Catal., B* **2011**, *110*, 286−295.
(22) Liang, N.; Wang, M.; Jin, L.; Huang, S. S.; Chen, W. L.; Xu, M.; He, Q. Q.; Zai, J. T.; Fang, N. H.; Qian, X. F. *ACS Appl. Mater. Interfaces* **2014**, *6*, 11698−11705.
(23) Liang, N.; Zai, J. T.; Xu, M.; Zhu, Q.; Wei, X.; Qian, X. F. *J. Mater. Chem. A* **2014**, *2*, 4208−4216.
(24) Zhang, W. D.; Sun, Y. J.; Dong, F.; Zhang, W.; Duan, S.; Zhang, Q. *Dalton. Trans.* **2014**, *43*, 12026−12036.
(25) Tian, N.; Huang, H. W.; Guo, Y. X.; He, Y.; Zhang, Y. H. A. *Appl. Surf. Sci.* **2014**, *322*, 249−254.
(26) Zhang, X. C.; Guo, T. Y.; Wang, X. W.; Wang, Y. W.; Fan, C. M.; Zhang, H. *Appl. Catal., B* **2014**, *150−151*, 486−495.
(27) Hu, D. D.; Zhang, K. Y.; Yang, Q.; Wang, M. J.; Xi, Y.; Hu, C. G. *Appl. Surf. Sci.* **2014**, *316*, 93−101.
(28) Lu, H. J.; Xu, L. L.; Wei, B.; Zhang, M. Y.; Gao, H.; Sun, W. J. *Appl. Surf. Sci.* **2014**, *303*, 360−366.
(29) Song, P. Y.; Xu, M.; Zhang, W. D. *Mater. Res. Bull.* **2015**, *62*, 88−95.
(30) Xu, Y. S.; Zhang, W. D. *Appl. Catal., B* **2013**, *140*, 306−316.
(31) Madhusudan, P.; Yu, J. G.; Wang, W. G.; Cheng, B.; Liu, G. *Dalton. Trans.* **2012**, *41*, 14345−14353.
(32) Zhang, Y. L.; Li, D. Y.; Zhang, Y. G.; Zhou, X. F.; Guo, S. J.; Yang, L. B. *J. Mater. Chem. A* **2014**, *2*, 8273−8280.
(33) Dong, F.; Li, Q. Y.; Zhou, Y.; Sun, Y. J.; Zhang, H. D.; Wu, Z. B. *Dalton Trans.* **2014**, *43*, 9468−9480.
(34) Dong, F.; Sun, Y. J.; Fu, M.; Ho, W.-K.; Lee, S. C.; Wu, Z. B. *Langmuir* **2012**, *28*, 766−773.
(35) Dong, F.; Xiong, T.; Wang, R.; Sun, Y. J.; Jiang, Y. K. *Dalton Trans.* **2014**, *43*, 6631−6642.
(36) Xiong, T.; Huang, H. W.; Sun, Y. J.; Dong, F. *J. Mater. Chem. A* **2015**, *3*, 6118−6127.
(37) Perdew, J. P.; Burke, K.; Ernzerhof, M. *Phys. Rev. Lett.* **1996**, *77*, 3865−3868.
(38) Segall, M. D.; Lindan, P. L. D.; Probert, M. J.; Pickard, C. J.; Hasnip, P. J.; Clark, S. J.; Payne, M. C. *J. Phys.: Condens. Matter* **2002**, *14*, 2717−2744.
(39) Ouyang, S. X.; Ye, J. H. *J. Am. Chem. Soc.* **2011**, *133*, 7757−7763.
(40) Shi, R.; Huang, G. L.; Lin, J.; Zhu, Y. F. *J. Phys. Chem. C* **2009**, *113*, 19633−19638.
(41) Guo, S.; Li, X. F.; Wang, H. Q.; Dong, F.; Wu, Z. B. *J. Colloid Interface Sci.* **2012**, *369*, 373−380.
(42) Windisch, C. F.; Exarhos, G. J.; Yao, C. H.; Wang, L. Q. *J. Appl. Phys.* **2007**, *101*, 123711−123717.
(43) Lv, Y. H.; Zhu, Y. Y.; Zhu, Y. F. *J. Phys. Chem. C* **2013**, *117*, 18520−18528.
(44) Tian, J.; Sang, Y. H.; Yu, G. W.; Jiang, H. D.; Mu, X. N.; Liu, H. *Adv. Mater.* **2013**, *25*, 5075−5080.
(45) Dong, F.; Wang, H. Q.; Wu, Z. B. *J. Phys. Chem. C* **2009**, *113*, 16717−16723.
(46) Li, Y. Y.; Liu, J. P.; Huang, X. T.; Yu, J. G. *Dalton Trans.* **2010**, *39*, 3420−3425.
(47) Ohko, Y.; Hashimoto, K.; Fujishima, A. *J. Phys. Chem. A* **1997**, *101*, 8057−8062.
(48) Wu, F.; Liu, Y. F.; Yu, G. X.; Shen, D. F.; Wang, Y. L.; Kan, E. J. *J. Phys. Chem. Lett.* **2012**, *3*, 3330−3334.
(49) Zhang, M.; Bai, X. J.; Liu, D.; Wang, J.; Zhu, Y. F. *Appl. Catal., B* **2015**, *164*, 77−81.
(50) Nasir, M.; Xi, Z. H.; Xing, M. Y.; Zhang, J. L.; Chen, F.; Tian, B. Z.; Bagwasi, S. *J. Phys. Chem. C* **2013**, *117*, 9520−9528.
(51) Kim, H.; Borse, P.; Choi, W.; Lee, J. *Angew. Chem., Int. Ed.* **2005**, *44*, 4585−4589.
(52) Hosseini, Z.; Taghavinia, N.; Sharifi, N.; Chavoshi, M.; Rahman, M. *J. Phys. Chem. C* **2008**, *112*, 18686−18689.
(53) Sun, S. M.; Wang, W. Z.; Zhang, L. *J. Phys. Chem. C* **2013**, *117*, 9113−9120.
(54) Kern, R.; Sastrawan, R.; Ferber, J.; Stangl, R.; Luther, J. *Electrochim. Acta* **2002**, *47*, 4213−4225.
(55) Wang, Y.; Wang, X. C.; Antonietti, M. *Angew. Chem., Int. Ed.* **2011**, *50*, 2−24.
(56) Huang, H. W.; He, Y.; He, R.; Lin, Z. S.; Zhang, Y. H.; Wang, S. C. *Inorg. Chem.* **2014**, *53*, 8114−8119.

DOI: 10.1021/acscatal.5b00444
ACS Catal. 2015, 5, 4094−4103